Geophysical Research Letters

RESEARCH LETTER
10.1029/2023GL105132

An Explanation for the Metric Dependence of the Midlatitude Jet-Waviness Change in Response to Polar Warming

Ruth Geen[1], Stephen I. Thomson[2], James A. Screen[2], Russell Blackport[3], Neil T. Lewis[2], Regan Mudhar[2], William J. M. Seviour[2], and Geoffrey K. Vallis[2]

[1]School of Geography, Earth and Environmental Sciences, University of Birmingham, Birmingham, UK, [2]Department of Mathematics and Statistics, University of Exeter, Exeter, UK, [3]Canadian Centre for Climate Modelling and Analysis, Environment and Climate Change Canada, Victoria, BC, Canada

Key Points:

- Spatial extent of midlatitude waves is increased by polar amplification
- Magnitudes of ridges and troughs within waves are decreased by polar amplification
- Accordingly, geometric, and anomaly-amplitude measures of jet waviness can yield opposing responses

Supporting Information:

Supporting Information may be found in the online version of this article.

Correspondence to:

R. Geen,
r.geen@bham.ac.uk

Citation:

Geen, R., Thomson, S. I., Screen, J. A., Blackport, R., Lewis, N. T., Mudhar, R., et al. (2023). An explanation for the metric dependence of the midlatitude jet-waviness change in response to polar warming. *Geophysical Research Letters*, *50*, e2023GL105132. https://doi.org/10.1029/2023GL105132

Received 22 JUN 2023
Accepted 20 OCT 2023

Author Contributions:

Conceptualization: Ruth Geen, Stephen I. Thomson, James A. Screen
Data curation: Ruth Geen
Formal analysis: Ruth Geen
Funding acquisition: Stephen I. Thomson, James A. Screen, William J. M. Seviour, Geoffrey K. Vallis
Investigation: Ruth Geen
Methodology: Ruth Geen, Stephen I. Thomson
Project Administration: Stephen I. Thomson, James A. Screen, William J. M. Seviour, Geoffrey K. Vallis
Resources: Ruth Geen
Software: Ruth Geen, Stephen I. Thomson, Russell Blackport

Abstract Arctic amplification has been proposed to promote temperature extremes by slowing the midlatitude jet and increasing the amplitude of its meanders. Observational and modeling studies have used a variety of metrics to quantify jet waviness. These studies show conflicting changes in jet waviness depending on the metric used and period examined. Here, we evaluate common metrics for dry idealized model simulations in which we apply polar warming of varying depth and meridional extent. In all simulations, polar warming increases the spatial extent of jet meanders, but reduces the magnitudes of ridges and troughs within the wave. As a result, geometric and anomaly-amplitude measures of jet waviness can yield opposing responses. This contrast between metrics is particularly evident when warming extends into the midlatitudes. In all simulations, midlatitude temperature anomalies weaken as the poles warm, suggesting that a wavier jet need not imply stronger temperature extremes.

Plain Language Summary The Arctic is warming faster than anywhere else on Earth, and this has been suggested to affect weather over midlatitude regions in Eurasia and North America. It has been proposed that, as the pole warms, the equator-to-pole temperature gradient is reduced and the atmospheric jet stream slows down and undergoes larger, slower-moving meanders, which bring long-lasting extreme temperatures. However, theories for understanding waves in the jet stream actually suggest that these waves could weaken when the equator-to-pole temperature gradient decreases. This study uses simple model simulations to test how different metrics for describing jet waviness respond when the pole is warmed. We find that the overall scale of meanders does seem to increase, but the associated temperature anomalies decrease, suggesting a wavier jet stream need not imply stronger temperature extremes.

1. Introduction

The Arctic has warmed four times faster than the rest of the world (Rantanen et al., 2022), motivating interest in how this might alter Northern Hemisphere midlatitude weather (e.g., Barnes & Screen, 2015; Cohen et al., 2014; Screen & Simmonds, 2013). One perspective that has garnered wide attention is that the weakening of the midlatitude temperature gradient, due to the faster warming of the Arctic than lower latitudes, results in a slower and more meandering or "wavier" jet stream. It is proposed that these meanders could generate more persistent and intense weather extremes (Francis & Vavrus, 2012). This hypothesis has become a mainstream public view (Hamilton & Lemcke-Stampone, 2014), but remains hotly debated by the scientific community (e.g., Blackport & Screen, 2020a; Cohen et al., 2020).

Reanalysis-based studies have suggested increases in jet waviness as the Arctic warms (Francis & Vavrus, 2015), although this depends on the period studied (Blackport & Screen, 2020b) and metric used (Screen & Simmonds, 2013). Identifying causality in reanalysis is complex, and it is important to recognize that correlation does not imply causation (Blackport & Screen, 2020a). Arctic amplification is not the only response to increased CO_2, with the tropics also experiencing warming that is most pronounced in the upper troposphere (e.g., Manabe & Wetherald, 1975). Arctic amplification itself arises via multiple processes, which include local sea-ice loss and poleward heat transport by midlatitude waves, as well as many local feedbacks that arise, for example, from changes to the vertical temperature gradient, or interactions with clouds and water vapor (e.g., Henry et al., 2021; Previdi et al., 2021; Screen et al., 2012).

Supervision: Stephen I. Thomson, James A. Screen, Geoffrey K. Vallis
Validation: Ruth Geen
Visualization: Ruth Geen, Stephen I. Thomson, Russell Blackport, Neil T. Lewis, Regan Mudhar, William J. M. Seviour, Geoffrey K. Vallis
Writing – original draft: Ruth Geen
Writing – review & editing: Ruth Geen, Stephen I. Thomson, James A. Screen, Russell Blackport, Neil T. Lewis, Regan Mudhar, William J. M. Seviour, Geoffrey K. Vallis

Even neglecting this complexity and considering polar warming as an independent climate forcing, it is not obvious that reducing the equator-to-pole temperature gradient should enhance midlatitude waves. From a basic fluid dynamics perspective, a smaller equator-to-pole temperature difference requires less transport of heat by midlatitude eddies (Shaw & Smith, 2022), and the weakened baroclinicity is expected to reduce generation of midlatitude wave activity (Wang et al., 2017). Intuition thus suggests that, considered alone, warming of the pole should reduce eddy activity. Consistent with this, idealized model simulations in which the equator-to-pole temperature gradient was systematically altered indicated a decrease in both wave amplitude and blocking frequency as the poles warmed (Hassanzadeh et al., 2014). However, it is worth noting that the spatial scale of jet meanders does not necessarily directly correspond to the magnitude of eddy anomalies advected (e.g., Xue et al., 2017), so that jet meandering may need to be considered as different to eddy magnitude.

In the idealized modeling work by Hassanzadeh et al. (2014), polar heating was simulated by reducing the equator-to-pole temperature gradient such that the forcing, and warming response, extended from the surface to the tropopause, and from the pole to the tropics. However, the observed Arctic Amplification signal is more focused over higher latitudes, with a vertical structure that extends upwards through the troposphere, varying in depth throughout the year (Graversen et al., 2008). In the atmospheric model response to sea-ice loss, warming is confined to high latitudes and lower levels (Deser et al., 2010). Recent model studies have compared responses to applied Arctic heating of different structures, mimicking the full Arctic response to CO_2 and the response to sea-ice loss. Results show that the mean midlatitude climate response to Arctic heating is sensitive to the structure of the applied warming (He et al., 2020; Kim et al., 2021; Labe et al., 2020; Sellevold et al., 2016; Yuval & Kaspi, 2020). A recent analysis of the response of jet-waviness to climate change in large ensembles of climate models suggests a decline in North Atlantic wave activity as the world warms, with North Pacific changes uncertain (Nie et al., 2023). The specific effect of polar warming structure on jet-waviness metrics is unknown.

Here, we analyze idealized model simulations in which we apply polar warming of different depths and meridional extents. We note that these simulations are artificial, taking polar warming as a given and neglecting the processes that drive it. Our aim is to identify the midlatitude response to a specified heating, allowing us to explore the hypothesized role of Arctic warming as a forcing for midlatitude changes. We show that the perceived change in jet meanders depends on the vertical and meridional structure of polar warming, and on the metric used to measure waviness.

2. Methods

2.1. Model Simulations

Simulations were run using the Isca idealized modeling framework (Vallis et al., 2018), based around the GFDL spectral dynamical core (Gordon & Stern, 1982). The control simulation replicates the Held-Suarez dry model configuration (Held & Suarez, 1994), with boundary-layer drag approximated by Rayleigh damping of the low-level winds and diabatic heating approximated by Newtonian relaxation to a prescribed equilibrium, perpetual equinox reference temperature, T_{eq}, that is a function of pressure, p, and latitude ϕ:

$$T_{eq} = \max\left\{200, \left[315 - (\Delta T)_y \sin^2\phi - (\Delta\theta)_z \log\left(\frac{p}{p_0}\right)\cos^2\phi\right]\left(\frac{p}{p_0}\right)^{\kappa}\right\}. \quad (1)$$

For all simulations, $(\Delta\theta)_z = 10$ K, $\kappa = \frac{2}{7}$, and $p_0 = 1{,}000$ mb. For the control simulation, the equator-to-pole equilibrium temperature difference, $(\Delta T)_y = 60$ K. All simulations were run with Earth's rotation rate. Although there is no diurnal or seasonal cycle in these simulations, we describe a day as a period of 86,400 s, and a year as a period of 360 days. The model was run at T85 horizontal resolution on 30 sigma levels, with a time-step of 600 s. Diagnostics were calculated at each time-step, with averages output at daily intervals. All data was interpolated to 20 evenly-spaced pressure levels in post-processing. Each simulation was run for 90 years, with the first 10 years discarded as spin-up and the remaining 80 used for analysis.

Two sets of simulations were performed. To allow comparison with previous work, the first set follows the methodology of Hassanzadeh et al. (2014). Temperatures over both poles were perturbed by altering the value of $(\Delta T)_y$ to values of 40 K (polar warming) and 80 K (polar cooling). The relaxation temperature profiles for each simulation are shown in Figures S1a–S1c in Supporting Information S1. The resulting heating extends

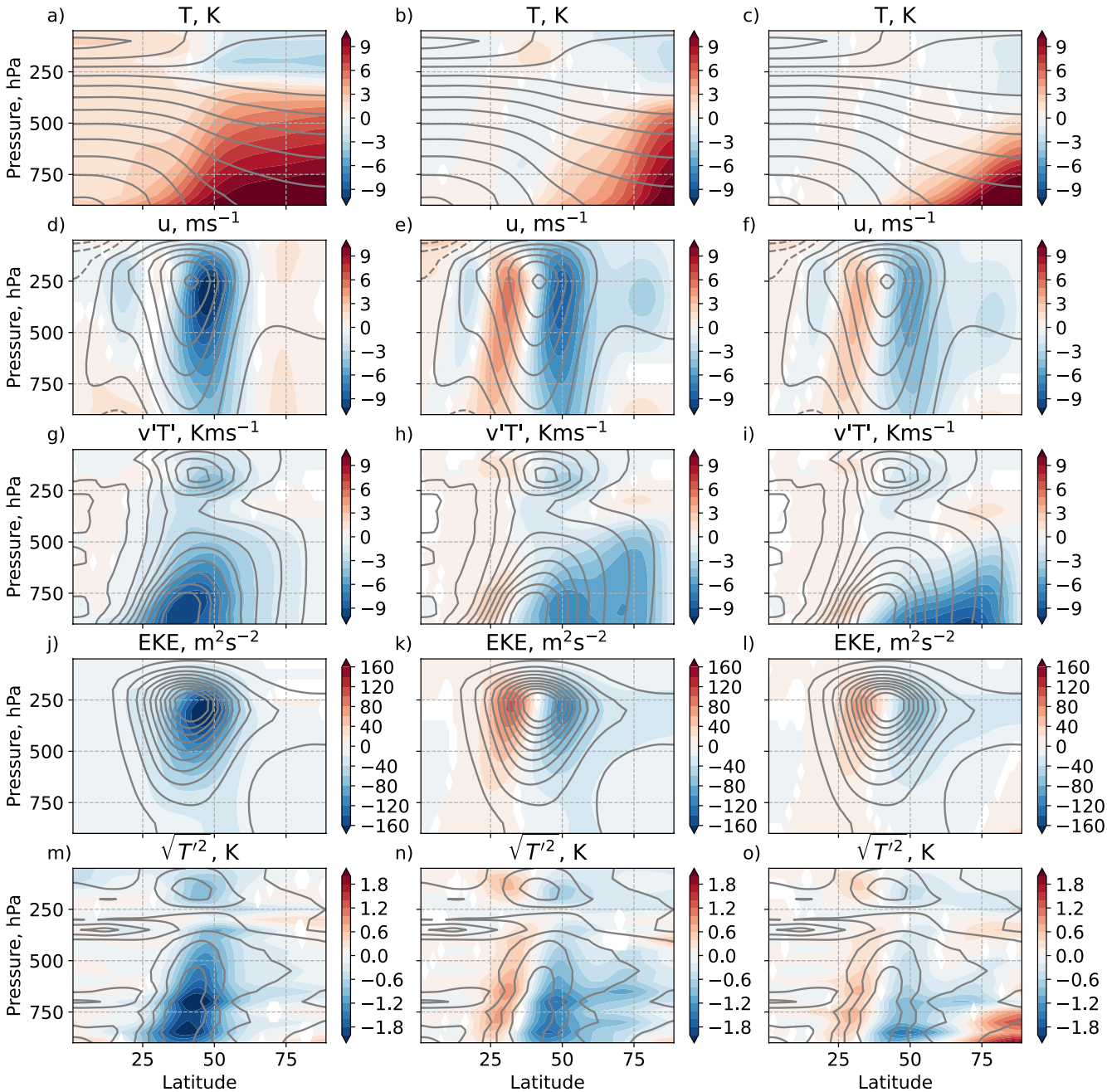

Figure 1. Control state (gray contours) and changes in zonal-mean quantities relative to the control (shading) for HKF40 (left column), OS400-4 (middle column), and OS800-4 (right column). From top to bottom, rows show: zonal-mean temperature (K), zonal windspeed (m s^{-1}), transient eddy heat flux (km s^{-1}), transient eddy kinetic energy (m^2 s^{-2}), and standard deviation of temperature (K). Welch's *t*-test is used to assess statistical significance, changes are plotted only where statistically different from 0 ($p < 0.05$). For the OS simulations, runs with heating of reference amplitude four are shown. Other amplitudes give qualitatively similar (but weaker) results.

throughout the depth of the troposphere and toward the tropics (e.g., Figure 1a). We use the author initials of Hassanzadeh et al. (2014) to denote these simulations HKF40 and HKF80 respectively.

The second set of simulations was designed to explore the effect of confining heating over the polar caps, and of altering the depth of the polar heating. A heating term was added over both poles in addition to the Newtonian relaxation to the control profile. The structure of this heating is based on that used in Orlanski and Solman (2010):

$$\frac{dT}{dt} = 0.5A\left(\frac{1000 - p_{ref}}{1000 - p_{top}}\right)\left(1 + \tanh\left(\frac{p - p_{top}}{p_{th}}\right)\right)e^{-\left(\frac{|\phi|-90}{y_w}\right)^2}. \quad (2)$$

This expression describes heating that follows a tanh function in pressure and a pole-centered Gaussian in latitude. $y_w = 15°$ sets the meridional decay length of the heating. In the vertical, the tanh function has a decay thickness of $p_{th} = 50$ hPa centered at p_{top}; that is, heating will extend from the surface and decay at p_{top}. The heating amplitude is set using the parameters A and p_{ref}. A sets the amplitude of the applied heating in K day^{-1} when $p_{top} = p_{ref} = 800$ hPa. By including p_{ref}, the heating amplitude decreases as its vertical depth increases, such that the integral of the heating from the surface to top of atmosphere remains constant. This ensures that the same total energy input is applied over the poles for a given value of A, allowing for cleaner comparisons between simulations with different heating depths. The resulting heating profiles are shown in Figures S1d–S1i in Supporting Information S1.

Simulations were run with p_{top} set to 400 and 800 hPa, and A set to 1, 2, and 4 K day^{-1}, so that combinations of p_{top} and A give six simulations in total. The author initials of Orlanski and Solman (2010) are used to denote these simulations as OSp_{top}-A. For example, OS800-1 would describe the simulation with heating extending from the surface to 800 hPa with an amplitude of 1 K day^{-1}. The temperature changes in simulations OS400-4 and OS800-4 can be seen in Figures 1b and 1c.

2.2. Waviness Metrics

We compare changes in multiple metrics that have been used to describe waviness of the midlatitude jet and circulation. All metrics were evaluated daily in both hemispheres at 500-hPa using either daily-mean windspeeds, or geopotential height, denoted Z500. Assuming gradient wind balance, the geopotential height isopleths provide a proxy for the orientation of the jet. With no seasonal cycle or topography, these simulations are symmetric about the equator, and results from both hemispheres were combined for analysis.

Specifically, we assess changes in:

1. Sinuosity (Cattiaux et al., 2016): the length of the Z500 isopleth corresponding to the average Z500 between 30° and 70°, including cut-off highs and lows, divided by the length of the 50° latitude circle.
2. Meridional wave amplitude (Hassanzadeh et al., 2014): the amplitude of a selected Z500 isopleth, excluding cut-off highs and lows, as evaluated from the first 15 Fourier components. Isopleths were selected following Hassanzadeh et al. (2014), and we additionally performed the calculation on the isopleth used to evaluate sinuosity.
3. Meridional circulation index (MCI, Francis & Vavrus, 2015): the ratio of the square of the meridional component of the wind to the square of the total windspeed at each grid cell.
4. Local wave activity (LWA, Chen et al., 2015; Huang & Nakamura, 2016), evaluated at each latitude and longitude by iterating over latitude and (a) finding the Z500 isopleth whose equivalent latitude matches the selected latitude, then (b) integrating the geopotential difference from this Z500 value over the area between the Z500 isopleth's actual and equivalent latitudes, including cut-off highs and lows.

The approaches used in evaluating each metric follow the papers referenced. For convenience, an overview of how each is calculated and a schematic summarizing their main features are provided in Supporting Information S1 (Text S1 and Figure S2).

Of the metrics listed above, only LWA accounts for the magnitude of geopotential height anomalies, as well as geometric effects. To assess the contribution of the anomaly magnitude versus the meridional extent of waves to LWA, we additionally define "LWA extent" (LWA-E), as the extent of the area over which LWA is evaluated.

3. Results

3.1. Zonal-Mean Changes

The focus of the present study is on changes in midlatitude wave characteristics across the simulations. However, it is informative to also briefly note the changes seen in zonal-mean characteristics typically used to study midlatitude processes. Figure 1 compares the changes in the zonal and time-mean climate when polar heating of different meridional extents and depths is applied. In all cases, a positive temperature anomaly is seen over the pole (top row), with the extent of the temperature anomaly corresponding to the extent of the imposed heating.

In HKF40, in which the meridional gradient of the relaxation temperature is reduced, temperature changes are strongest over the pole and near the surface, but changes extend from the pole to the tropics, and throughout the depth of the troposphere. The reduction in the midlatitude temperature gradient is associated with a decrease in zonal wind strength (Figure 1d), consistent with thermal wind balance. The reduced equator-to-pole temperature gradient and resultant reduced baroclinicity lead to a decrease in meridional transient eddy heat flux, transient eddy kinetic energy and standard deviation of temperature (Figures 1g, 1j, and 1m). Note that in these idealized simulations there are no zonally asymmetric boundary conditions to support stationary eddies, and transient eddies are here defined as deviations from the time and zonal mean.

In OS400-4 and OS800-4, in which heating is confined over the pole, a slightly different response is seen. Temperature changes are strongest in the warmed region, which no longer extends into the tropics. A slight increase in temperature is also seen at around 25°, with decreases in temperature elsewhere. The midlatitude jet and eddy kinetic energy maximum shift equatorward, and the eddy heat flux decreases in both simulations, with the strongest decreases co-located with the strongest temperature anomaly gradients. This equatorward jet shift in OS400-4 and OS800-8 is similar to the response to sea-ice loss seen in coupled models (Screen et al., 2018) and the Polar Amplification Model Intercomparison Project ensemble (Smith et al., 2022).

Note that all simulations show a decrease in eddy heat flux, eddy kinetic energy and temperature variations northward of the jet core. This matches what could be expected from intuition: with a reduced equator-to-pole temperature gradient there is less requirement for transport of heat by transient eddies from warmed to cooled regions of the globe, and reduced baroclinic instability to generate Rossby waves, so that midlatitude eddy heat transport weakens accordingly. However, a reduction in eddy activity as assessed from an eddy/mean-state decomposition does not preclude changes in jet-waviness as defined as the scale of meanders in the jet, as we discuss below.

3.2. Changes in Waviness

Although eddy/mean-state decomposition (e.g., lower three rows of Figure 1) shows a reduction in midlatitude eddy activity as the poles are warmed, we find that the waviness metrics give a different picture. For each metric listed in Section 2.2, the left column of Figure 2 shows the average value over time, longitude and both hemispheres for each simulation. To allow all sets of simulations to be plotted on the same axis, we define an Arctic Amplification Index (AAI) as the average 850-hPa temperature over the polar caps (65–90°N and S) minus the global average temperature (cf. Blackport & Screen, 2020b). The right column of Figure 2 shows the spread of values measured for selected simulations as density histograms.

In all simulations, sinuosity increases as the poles warm (Figure 2a). This increase is stronger in the OS400 and HKF simulations, where heating extends further upwards through the atmosphere and so has a greater impact at 500 hPa. The corresponding histograms (Figure 2b) show that polar warming is associated with an increase in the average sinuosity, and a marked increase in the spread of values measured, with higher values occurring more frequently.

For meridional wave amplitude, the crosses in Figure 2c show the values obtained for the isopleth corresponding to the time and zonal-mean Z500 at the latitude of maximum time and zonal-mean 500-hPa zonal wind (denoted Z1 in Hassanzadeh et al., 2014). For this isopleth choice, this metric does not show robust, monotonic changes across the OS400 and OS800 simulations. Stronger changes are seen in the HKF simulations, with wave amplitude decreasing overall with increased AAI, consistent with Hassanzadeh et al. (2014). Similar results are found for other isopleth choices used by Hassanzadeh et al. (2014), shown in Figures S3–S5 in Supporting Information S1.

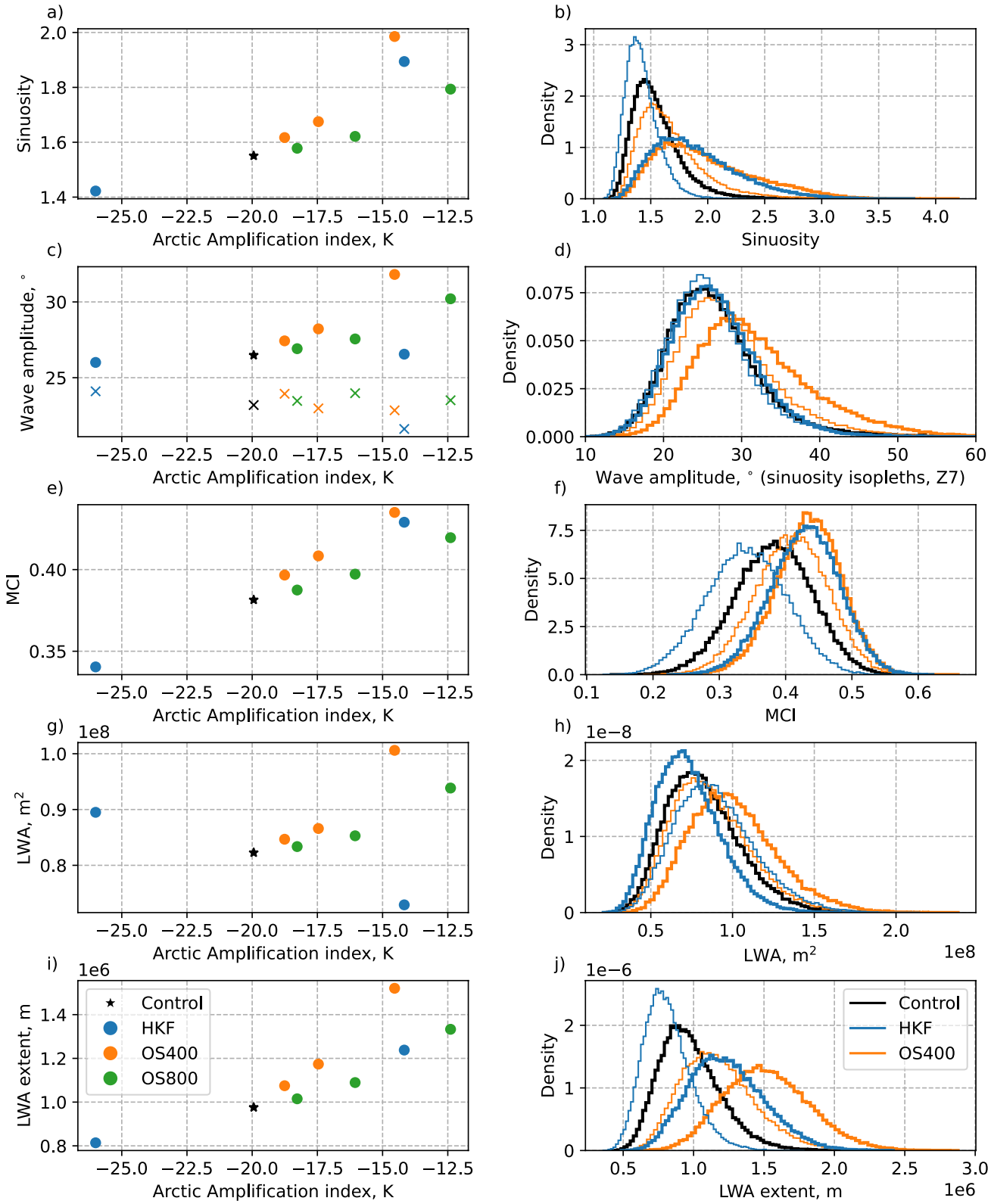

Figure 2.

In contrast, when meridional wave amplitude is evaluated using the isopleth used to calculate sinuosity for each day (i.e., daily average Z500 between 30° and 70°), an increase is seen with AAI across all simulations (circles in Figure 2c). The increase in meridional wave amplitude is strongest for the OS400 series of simulations and is weak for the HKF simulations. We note that the range spanned by the histogram of sinuosity isopleth values in each simulation aligns with the spread of isopleth choices used by Hassanzadeh et al. (2014) in each simulation (compare Figures S2b, S4b, and S6 in Supporting Information S1). This suggests that rather than using a single average isopleth to assess waviness, a daily isopleth choice may more appropriately characterize the situation on a given day. Regardless of the isopleth chosen to characterize meridional wave amplitude, the change in the distribution of values is much more moderate across simulations than for other metrics (Figure 2d, Figures S3–S5 in Supporting Information S1).

MCI increases with the AAI in all simulations. As with sinuosity, the increase in MCI with AAI is strongest for the OS400 simulations, where heating extends higher up in the atmosphere. Overall, the change in mean MCI values follows a similar pattern to that seen for sinuosity. However, the histogram changes show differences in behavior between the two metrics. For MCI, histograms show a shift in the density distribution to higher values, as seen for sinuosity, but this is associated with a slight narrowing, rather than broadening, of the distribution. This is likely due to the difference in formulation of the two metrics, sinuosity has a lower limit of 1, but no clear upper limit. In contrast, for MCI to take large values in the zonal mean, the local meridional windspeed needs to approach the magnitude of the local zonal windspeed. For all simulations, values appear to taper off at ∼0.6, suggesting some upper limit on how meridional the flow can become.

For LWA, the response to polar warming strongly differs depending on the warming structure (Figure 2g). In the HKF simulations, although other metrics increase as the poles warm, LWA decreases, with the corresponding histograms showing a decrease in values across the distribution. The opposite behavior is seen in the OS400 and OS800 simulations, with polar warming linked to an increase in LWA. As with sinuosity and meridional wave amplitude, the increase is stronger for deeper warming.

While sinuosity and meridional wave amplitude assess only the geometric structure of a selected isopleth, LWA additionally accounts for the magnitude of geopotential anomalies within midlatitude waves. To reconcile the difference in behavior between LWA and sinuosity in the HKF simulations, we isolate the geometric component of LWA by evaluating the spatial extent that is integrated over when calculating LWA, which we denote LWA extent, LWA-E. Similarly to sinuosity, average LWA-E increases with polar warming across all simulations (Figure 2i), and the distribution of values broadens (Figure 2j).

Figures 2g–2j imply that LWA-E makes a dominant contribution to LWA for the OS400 and OS800 simulations, while changes in the magnitude of geopotential anomalies dominate LWA for the HKF simulations. This difference can be understood from the changes in the 500-hPa meridional gradient of geopotential height, shown in Figures 3a and 3e. In both sets of simulations, polar warming decreases the magnitude of the geopotential gradient, and shifts the peak value equatorward. The decrease in geopotential gradient is stronger in the HKF simulations, where the applied warming (HKF40) or cooling (HKF80) extends throughout the midlatitudes and into the tropics. In the OS simulations the decrease in meridional geopotential gradient is comparatively weak.

Considering waves as stirring motions mixing some average background geopotential gradient, it can be expected that an enhanced geopotential gradient will mean that air parcels advected north or south as the wave meanders will differ more strongly in geopotential from those at their new latitude, leading to larger magnitude geopotential anomalies. In this perspective, a simple dimensional analysis (Chen et al., 2015; Xue et al., 2017) can be used to relate the LWA to the scale of motions, η and meridional geopotential gradient as:

$$LWA \sim \frac{1}{2}\eta^2 \frac{dz}{dy}. \tag{3}$$

Figure 2. Differences in values of waviness metrics across simulations. For a given metric, the left column shows the time-means for each simulation, while the right column shows density histograms for the control (black), HKF80 (thin blue), HKF40 (thick blue), OS400-2 (thin orange), and OS400-4 (thick orange). From top to bottom, rows show: sinuosity (Cattiaux et al., 2016), wave amplitude (Hassanzadeh et al., 2014), MCI (Francis & Vavrus, 2015), LWA (Chen et al., 2015), and the LWA-E. Values of MCI, LWA, and LWA-E are averaged between 40° and 60° North and South. Panel (c) shows meridional wave amplitude evaluated for isopleths corresponding to the time and zonal-mean Z500 at the latitude of maximum time and zonal-mean 500-hPa zonal wind (crosses) and the sinuosity isopleth (filled circles); histograms in Panel (d) are for the sinuosity isopleth.

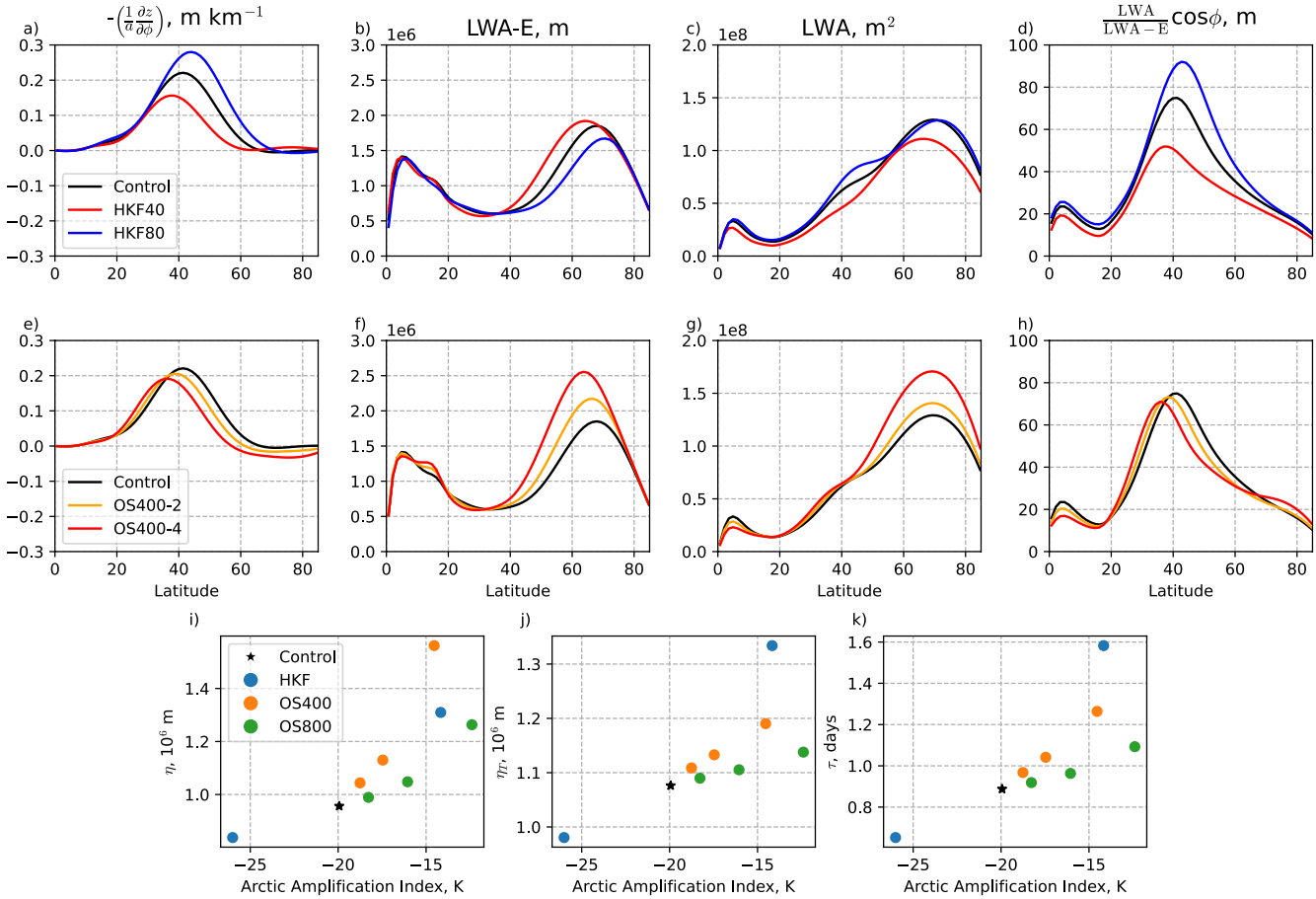

Figure 3. From left to right, columns of the top two rows show time and zonal-mean latitudinal structure of: meridional gradient of 500-hPa geopotential height (a, e), local wave activity (LWA) extent (b, f), LWA (c, g), and LWA divided by LWA extent (d, h). Note that the latter is multiplied by cosϕ to help in comparison with the zonal-mean meridional geopotential gradient. Top row shows HFK experiments, middle row shows OS400 experiments. The lower row shows simple scalings characterizing changes seen in the upper rows: length scales characterizing the meridional displacement of (i) 500-hPa height contours and (j) 500-hPa temperature contours, and (k) an estimated timescale associated with anomaly persistence. The scaling values shown are averages between 40° and 55°, poleward of this the small geopotential and temperature gradients lead to the length and timescales becoming poorly defined.

The length scale, η, has been evaluated for all simulations and is plotted against AAI in Figure 3i, and shows broadly similar behavior to LWA-E. We note that here, for ease of calculation and comparison to Figures 3a and 3e, we evaluate η using the gradient of geopotential height with respect to latitude, while Xue et al. (2017) use equivalent latitude.

Figure 3b shows the zonal and time-mean LWA-E for the HKF simulations. There is a moderate increase in midlatitude LWA-E as the poles warm, implying an increase in the meridional scale of the waves that are mixing air across the geopotential gradient. However, this is accompanied by a strong decrease in the meridional geopotential gradient (Figure 3a). The latter factor dominates for these simulations, giving an overall decrease in LWA (Figure 3c).

Figure 3d shows the ratio of LWA to LWA-E, indicating the average magnitude of geopotential anomalies that comprise the LWA. This ratio follows a similar structure to that of the meridional gradient of geopotential height, consistent with anomaly magnitude at each latitude being determined by geopotential gradient, cf. the simple scaling in Equation 3.

Similar to the HKF simulations, in the OS400 simulations the geopotential gradient decreases (Figure 3e) and LWA-E increases (Figure 3f) as the pole warms. However, in this case, the geometric increase in wave-size outweighs the reduced anomaly magnitude, leading to increased LWA (Figure 3g). Again, the ratio of LWA to LWA-E follows a similar structure to the geopotential gradient (Figure 3h).

A characteristic length scale can also be identified for temperature anomalies, $\eta_T \sim -T'/\frac{dT}{dy}$. Values of η_T for each simulation were evaluated at each latitude using the 500-hPa temperature standard deviation and meridional temperature gradient, latitudinal averages are shown in Figure 3j. Although the precise values differ to η, the two length scales both show increases across simulations as the poles warm. One notable difference is that the strong reduction to the midlatitude temperature gradient in HKF40 leads to a larger increase in η_T than might be estimated from η. Nonetheless, this scaling helps to reconcile the reduction in temperature standard deviation seen in Figure 1 with the increased meander extent with polar warming that was identified in Section 3.2. The meridional temperature gradient decreases as the pole warms, but the spatial scale of north-south motions increases. The reduction in temperature gradient dominates in the midlatitudes in all simulations, leading to reduced midlatitude temperature standard deviation.

Figure 3k estimates a change in timescale associated with the persistence of temperature anomalies: $\tau = \frac{\eta_T}{v'}$. This is evaluated using the standard deviation of 500-hPa meridional wind. As the pole warms, η_T increases while EKE decreases, and accordingly τ increases in magnitude. This suggests that anomalies may become slower to develop and decay, potentially implying an increase in lifetime of temperature anomalies. Full exploration of anomaly persistence is left for future work.

4. Conclusions

Here, we have assessed the behavior of five different measures of atmospheric waviness across idealized simulations with differing structures of polar warming. In all simulations, we find that polar warming increases the spatial extent of jet meanders, but reduces the magnitudes of ridges and troughs within the wave. As a result, for a given warming structure, geometric and anomaly-amplitude measures of jet waviness can yield opposing responses. Meanwhile, for a single metric, specifically LWA, different warming structures may generate opposite-signed changes.

Despite these differences, once consideration is given to what each metric measures, a coherent picture emerges that is robust across these dry simulations. Metrics that assess changes in the geometric scale of midlatitude waves (e.g., sinuosity, LWA-E) show an increase under polar warming in all simulations. Decreases in the magnitude of anomalies advected are largest where the midlatitude geopotential gradient is most strongly reduced. For LWA, which combines both anomaly amplitude and geometric effects, this can result in apparently contradictory results, with the overall change depending on whether the increased spatial scale or reduced anomaly amplitude dominates.

We note that these simulations are highly idealized. Although they shed some light on the differing responses across waviness metrics, patterns seen here may not directly map onto real-world observed behavior. In particular, our simulations have been designed to target the polar-amplification signal and assess the hypothesis that this will give increased midlatitude waviness. They do not include the mid-tropospheric tropical warming signature of climate change, which also influence midlatitude eddy behavior (e.g., Butler et al., 2010; Yuval & Kaspi, 2020). More complex, fully coupled simulations show that the mean midlatitude circulation response to sea-ice loss or Arctic amplification is very different to the response to global warming (e.g., Blackport & Kushner, 2017; Hay et al., 2022; McCusker et al., 2017). The polar heating applied here (~10 K) is large compared to that observed (~2 K observed Rantanen et al., 2022). Our simulations also do not include zonal asymmetries in either the base state or the warming structure, which could amplify stationary or transient wave activity locally. The model is dry and includes only a very simple approximation of atmospheric physics, a full description of radiative processes and latent heat release might modify the responses seen.

Keeping the above limitations in mind, our results emphasize that careful thought is needed in understanding any relationship between a given waviness metric and impacts. In line with intuition and results from previous work (Screen, 2014), we find that warmer polar temperatures do not result in an increased magnitude of temperature standard deviation (e.g., Figures 1m–1o). However, we do find an increase in the geometric scale of waves, and there is a preliminary indication that the timescale of these waves may increase with polar warming (Figure 3k). It is possible that a warmer pole might result in a larger spatial scale of weaker-magnitude and longer-lived wave anomalies, so that a larger area, or multiple areas, might potentially be affected simultaneously. Whether such changes would lead to any significant impacts is not clear.

Data Availability Statement

Simulations were run with the Isca modelling framework, free to install at https://github.com/ExeClim/Isca. The specific commit used is at https://doi.org/10.5281/zenodo.8338042 (Vallis et al., 2023).

The time mean averaged data used in Figures 1 and 3, and time series of waviness metrics used in Figure 2 are available at https://doi.org/10.25500/edata.bham.00000958 (Geen, 2023).

Acknowledgments
This work was supported by the Natural Environment Research Council (Grant NE/V005855/1). We thank the two anonymous reviewers for their helpful comments on the manuscript, and for the suggestion to evaluate the scalings shown in Figures 3i–3k.

References

Barnes, E. A., & Screen, J. A. (2015). The impact of Arctic warming on the midlatitude jet-stream: Can it? Has it? Will it? *Wiley Interdisciplinary Reviews: Climate Change*, *6*(3), 277–286. https://doi.org/10.1002/wcc.337

Blackport, R., & Kushner, P. J. (2017). Isolating the atmospheric circulation response to arctic sea ice loss in the coupled climate system. *Journal of Climate*, *30*(6), 2163–2185. https://doi.org/10.1175/JCLI-D-16-0257.1

Blackport, R., & Screen, J. A. (2020a). Insignificant effect of Arctic amplification on the amplitude of midlatitude atmospheric waves. *Science Advances*, *6*(8), eaay2880. https://doi.org/10.1126/sciadv.aay2880

Blackport, R., & Screen, J. A. (2020b). Weakened evidence for mid-latitude impacts of Arctic warming. *Nature Climate Change*, *10*(12), 1065–1066. https://doi.org/10.1038/s41558-020-00954-y

Butler, A. H., Thompson, D. W. J., & Heikes, R. (2010). The steady-state atmospheric circulation response to climate change–like thermal forcings in a simple general circulation model. *Journal of Climate*, *23*(13), 3474–3496. https://doi.org/10.1175/2010JCLI3228.1

Cattiaux, J., Peings, Y., Saint-Martin, D., Trou-Kechout, N., & Vavrus, S. J. (2016). Sinuosity of midlatitude atmospheric flow in a warming world. *Geophysical Research Letters*, *43*(15), 8259–8268. https://doi.org/10.1002/2016gl070309

Chen, G., Lu, J., Burrows, D. A., & Leung, L. R. (2015). Local finite-amplitude wave activity as an objective diagnostic of midlatitude extreme weather. *Geophysical Research Letters*, *42*(24), 10–952. https://doi.org/10.1002/2015gl066959

Cohen, J., Screen, J. A., Furtado, J. C., Barlow, M., Whittleston, D., Coumou, D., et al. (2014). Recent Arctic amplification and extreme mid-latitude weather. *Nature Geoscience*, *7*(9), 627–637. https://doi.org/10.1038/ngeo2234

Cohen, J., Zhang, X., Francis, J., Jung, T., Kwok, R., Overland, J., et al. (2020). Divergent consensuses on Arctic amplification influence on midlatitude severe winter weather. *Nature Climate Change*, *10*(1), 20–29. https://doi.org/10.1038/s41558-019-0662-y

Deser, C., Tomas, R., Alexander, M., & Lawrence, D. (2010). The seasonal atmospheric response to projected Arctic sea ice loss in the late twenty-first century. *Journal of Climate*, *23*(2), 333–351. https://doi.org/10.1175/2009JCLI3053.1

Francis, J. A., & Vavrus, S. J. (2012). Evidence linking Arctic amplification to extreme weather in mid-latitudes. *Geophysical Research Letters*, *39*(6), L06801. https://doi.org/10.1029/2012gl051000

Francis, J. A., & Vavrus, S. J. (2015). Evidence for a wavier jet stream in response to rapid arctic warming. *Environmental Research Letters*, *10*(1), 014005. https://doi.org/10.1088/1748-9326/10/1/014005

Geen, R. (2023). Research data supporting the publication 'An explanation for the metric dependence of the midlatitude jet waviness change in response to polar warming' [Dataset]. UBIRA. https://doi.org/10.25500/edata.bham.00000958

Gordon, C. T., & Stern, W. F. (1982). A description of the GFDL global spectral model. *Monthly Weather Review*, *110*(7), 625–644. https://doi.org/10.1175/1520-0493(1982)110<0625:adotgg>2.0.co;2

Graversen, R. G., Mauritsen, T., Tjernström, M., Källén, E., & Svensson, G. (2008). Vertical structure of recent arctic warming. *Nature*, *451*(7174), 53–56. https://doi.org/10.1038/nature06502

Hamilton, L. C., & Lemcke-Stampone, M. (2014). Arctic warming and your weather: Public belief in the connection. *International Journal of Climatology*, *34*(5), 1723–1728. https://doi.org/10.1002/joc.3796

Hassanzadeh, P., Kuang, Z., & Farrell, B. F. (2014). Responses of midlatitude blocks and wave amplitude to changes in the meridional temperature gradient in an idealized dry GCM. *Geophysical Research Letters*, *41*(14), 5223–5232. https://doi.org/10.1002/2014gl060764

Hay, S., Kushner, P. J., Blackport, R., McCusker, K. E., Oudar, T., Sun, L., et al. (2022). Separating the influences of low-latitude warming and sea ice loss on northern hemisphere climate change. *Journal of Climate*, *35*(8), 2327–2349. https://doi.org/10.1175/jcli-d-21-0180.1

He, S., Xu, X., Furevik, T., & Gao, Y. (2020). Eurasian cooling linked to the vertical distribution of Arctic warming. *Geophysical Research Letters*, *47*(10), e2020GL087212. https://doi.org/10.1029/2020gl087212

Held, I. M., & Suarez, M. J. (1994). A proposal for the intercomparison of the dynamical cores of atmospheric general circulation models. *Bulletin of the American Meteorological Society*, *75*(10), 1825–1830. https://doi.org/10.1175/1520-0477(1994)075<1825:apftio>2.0.co;2

Henry, M., Merlis, T. M., Lutsko, N. J., & Rose, B. E. (2021). Decomposing the drivers of polar amplification with a single-column model. *Journal of Climate*, *34*(6), 2355–2365. https://doi.org/10.1175/jcli-d-20-0178.1

Huang, C. S., & Nakamura, N. (2016). Local finite-amplitude wave activity as a diagnostic of anomalous weather events. *Journal of the Atmospheric Sciences*, *73*(1), 211–229. https://doi.org/10.1175/jas-d-15-0194.1

Kim, D., Kang, S. M., Merlis, T. M., & Shin, Y. (2021). Atmospheric circulation sensitivity to changes in the vertical structure of polar warming. *Geophysical Research Letters*, *48*(19), e2021GL094726. https://doi.org/10.1029/2021gl094726

Labe, Z., Peings, Y., & Magnusdottir, G. (2020). Warm Arctic, cold Siberia pattern: Role of full Arctic amplification versus sea ice loss alone. *Geophysical Research Letters*, *47*(17), e2020GL088583. https://doi.org/10.1029/2020gl088583

Manabe, S., & Wetherald, R. T. (1975). The effects of doubling the CO_2 concentration on the climate of a general circulation model. *Journal of the Atmospheric Sciences*, *32*(1), 3–15. https://doi.org/10.1175/1520-0469(1975)032<0003:teodtc>2.0.co;2

McCusker, K. E., Kushner, P. J., Fyfe, J. C., Sigmond, M., Kharin, V. V., & Bitz, C. M. (2017). Remarkable separability of circulation response to arctic sea ice loss and greenhouse gas forcing. *Geophysical Research Letters*, *44*(15), 7955–7964. https://doi.org/10.1002/2017gl074327

Nie, Y., Chen, G., Lu, J., Zhou, W., & Zhang, Y. (2023). Constraining the varied response of Northern Hemisphere winter circulation waviness to climate change. *Geophysical Research Letters*, *50*(6), e2022GL102150. https://doi.org/10.1029/2022gl102150

Orlanski, I., & Solman, S. (2010). The mutual interaction between external Rossby waves and thermal forcing: The subpolar regions. *Journal of the Atmospheric Sciences*, *67*(6), 2018–2038. https://doi.org/10.1175/2010jas3267.1

Previdi, M., Smith, K. L., & Polvani, L. M. (2021). Arctic amplification of climate change: A review of underlying mechanisms. *Environmental Research Letters*, *16*(9), 093003. https://doi.org/10.1088/1748-9326/ac1c29

Rantanen, M., Karpechko, A. Y., Lipponen, A., Nordling, K., Hyvärinen, O., Ruosteenoja, K., et al. (2022). The Arctic has warmed nearly four times faster than the globe since 1979. *Communications Earth & Environment*, *3*(1), 168. https://doi.org/10.1038/s43247-022-00498-3

Screen, J. A. (2014). Arctic amplification decreases temperature variance in northern mid-to high-latitudes. *Nature Climate Change*, *4*(7), 577–582. https://doi.org/10.1038/nclimate2268

Screen, J. A., Deser, C., & Simmonds, I. (2012). Local and remote controls on observed Arctic warming. *Geophysical Research Letters*, *39*(10), L10709. https://doi.org/10.1029/2012gl051598

Screen, J. A., Deser, C., Smith, D. M., Zhang, X., Blackport, R., Kushner, P. J., et al. (2018). Consistency and discrepancy in the atmospheric response to arctic sea-ice loss across climate models. *Nature Geoscience*, *11*(3), 155–163. https://doi.org/10.1038/s41561-018-0059-y

Screen, J. A., & Simmonds, I. (2013). Exploring links between Arctic amplification and mid-latitude weather. *Geophysical Research Letters*, *40*(5), 959–964. https://doi.org/10.1002/grl.50174

Sellevold, R., Sobolowski, S., & Li, C. (2016). Investigating possible Arctic-midlatitude teleconnections in a linear framework. *Journal of Climate*, *29*(20), 7329–7343. https://doi.org/10.1175/jcli-d-15-0902.1

Shaw, T. A., & Smith, Z. (2022). The midlatitude response to polar sea ice loss: Idealized slab-ocean aquaplanet experiments with thermodynamic sea ice. *Journal of Climate*, *35*(8), 1–50. https://doi.org/10.1175/jcli-d-21-0508.1

Smith, D. M., Eade, R., Andrews, M., Ayres, H., Clark, A., Chripko, S., et al. (2022). Robust but weak winter atmospheric circulation response to future arctic sea ice loss. *Nature Communications*, *13*(1), 727. https://doi.org/10.1038/s41467-022-28283-y

Vallis, G. K., Colyer, G., Geen, R., Gerber, E., Jucker, M., Maher, P., et al. (2018). Isca, v1.0: A framework for the global modelling of the atmospheres of Earth and other planets at varying levels of complexity. *Geoscientific Model Development*, *11*(3), 843–859. https://doi.org/10.5194/gmd-11-843-2018

Vallis, G. K., Colyer, G., Geen, R., Gerber, E., Jucker, M., Maher, P., et al. (2023). Isca, v1.0: A framework for the global modelling of the atmospheres of Earth and other planets at varying levels of complexity. Commit c1e14e8 [Software]. Zenodo. https://doi.org/10.5281/zenodo.8338042

Wang, J., Kim, H.-M., & Chang, E. K. (2017). Changes in Northern Hemisphere winter storm tracks under the background of Arctic amplification. *Journal of Climate*, *30*(10), 3705–3724. https://doi.org/10.1175/jcli-d-16-0650.1

Xue, D., Lu, J., Sun, L., Chen, G., & Zhang, Y. (2017). Local increase of anticyclonic wave activity over northern Eurasia under amplified Arctic warming. *Geophysical Research Letters*, *44*(7), 3299–3308. https://doi.org/10.1002/2017gl072649

Yuval, J., & Kaspi, Y. (2020). Eddy activity response to global warming-like temperature changes. *Journal of Climate*, *33*(4), 1381–1404. https://doi.org/10.1175/jcli-d-19-0190.1

References From the Supporting Information

Hijmans, R. J. (2021). geosphere: Spherical Trigonometry (Computer software manual). (R package version 1.5–14). Retrieved from https://CRAN.R-project.org/package=geosphere

Nakamura, N., & Zhu, D. (2010). Finite-amplitude wave activity and diffusive flux of potential vorticity in eddy–mean flow interaction. *Journal of the Atmospheric Sciences*, *67*(9), 2701–2716. https://doi.org/10.1175/2010jas3432.1